



HAL
open science

Trace elements discriminate between tissues in highly weathered fossils

Pierre Gueriau, Farid Saleh, Lukáš Laibl, Francesc Perez Peris, Lorenzo Lustri, Cristian Mocuta, Solenn Réguer, Serge X. Cohen, Loïc Bertrand, Allison C Daley

► **To cite this version:**

Pierre Gueriau, Farid Saleh, Lukáš Laibl, Francesc Perez Peris, Lorenzo Lustri, et al.. Trace elements discriminate between tissues in highly weathered fossils. 2023. hal-04230408

HAL Id: hal-04230408

<https://hal.science/hal-04230408>

Preprint submitted on 5 Oct 2023

HAL is a multi-disciplinary open access archive for the deposit and dissemination of scientific research documents, whether they are published or not. The documents may come from teaching and research institutions in France or abroad, or from public or private research centers.

L'archive ouverte pluridisciplinaire **HAL**, est destinée au dépôt et à la diffusion de documents scientifiques de niveau recherche, publiés ou non, émanant des établissements d'enseignement et de recherche français ou étrangers, des laboratoires publics ou privés.



Distributed under a Creative Commons Attribution 4.0 International License

1 **Trace elements discriminate between tissues in highly weathered** 2 **fossils**

3
4 **Pierre Gueriau^{a,b,1}, Farid Saleh^{a,1}, Lukáš Laibl^{a,c,d}, Francesc Perez Peris^a, Lorenzo Lustri^a,**
5 **Cristian Mocuta^e, Solenn Réguer^e, Serge X. Cohen^b, Loïc Bertrand^f, and Allison C. Daley^{a,1}**
6

7 ^aInstitute of Earth Sciences, University of Lausanne, Géopolis, CH-1015 Lausanne, Switzerland;

8 ^bUniversité Paris-Saclay, CNRS, ministère de la Culture, UVSQ, MNHN, Institut photonique
9 d'analyse non-destructive européen des matériaux anciens, 91192, Saint-Aubin, France;

10 ^cCzech Academy of Sciences, Institute of Geology, Rozvojová 269, 165 00 Prague 6, Czech
11 Republic;

12 ^dInstitute of Geology and Palaeontology, Faculty of Science, Charles University, Albertov 6,
13 Prague, 12843, Czech Republic;

14 ^eSynchrotron SOLEIL, l'Orme des Merisiers, Départementale 128, 91190 Saint-Aubin, France;

15 ^fUniversité Paris-Saclay, ENS Paris-Saclay, CNRS, Photophysique et Photochimie
16 Supramoléculaires et Macromoléculaires, 91190 Gif-sur-Yvette, France.

17
18 ¹To whom correspondence may be addressed. Emails: pierre.gueriau@hotmail.fr,
19 farid.nassim.saleh@gmail.com, or allison.daley@unil.ch

20
21 **Author Contributions:** P.G. and A.C.D. designed the research; P.G., F.S., L.La., F.P.P., L.Lu.
22 C.M. and S.R. performed the research; P.G., C.M., S.R., S.X.C. and L.B. contributed new
23 reagents/analytic tools; P.G., F.S., S.X.C. and L.B. analysed data; P.G. and F.S. wrote the paper
24 with input from all authors.

25
26 **Keywords:** Ordovician | Fezouata Biota | synchrotron X-ray fluorescence | taphonomy | nervous
27 system

28
29 **ORCID**

30 PG, 0000-0002-7529-3456; FS, 0000-0002-7529-3456; LLa, 0000-0001-9049-3811; FPP, 0000-
31 0002-4526-9308; LLu, 0000-0002-8951-5160; CM, 0000-0001-5540-449X; SR, 0000-0002-7449-
32 0503; SXC, 0000-0003-2435-2417; LB, 0000-0001-6622-9113; ACD, 0000-0001-5369-5879

33

34 **Abstract**

35 **Palaeontologists assess the affinities of fossils using either morphology-based phylogenetic**
36 **analyses, possibly enhanced by the use of advanced imaging techniques, or the identification**
37 **of remnants or derivatives of fossil organic molecules with high taxonomic specificity**
38 **(“biomarkers”). However, these approaches are often of little use for the majority of fossils**
39 **whose original morphology and chemistry have been severely altered or completely lost**
40 **during decay, diagenesis and modern weathering. Here we show that the inorganic**
41 **incorporation of trace elements during fossilization and diagenesis can be used to assess the**
42 **affinity of highly altered fossils, constituting a powerful tool overlooked so far. This is**
43 **illustrated by the study of a wide range of animals from the Early Ordovician Fezouata Shale**
44 **(Tremadocian, Morocco) using synchrotron X-ray fluorescence major-to-trace elemental**
45 **mapping. Although all fossils studied here have turned into iron oxides, spectral analyses**
46 **reveal that their different tissue types (i.e. biomineralised, sclerotised, cuticularised, and**
47 **internal tissues) can be distinguished on the basis of their trace element inventories. The**
48 **resulting elemental classes and distributions allowed us to identify an enigmatic, highly**
49 **weathered organism as a new stem euarthropod preserving remains of its nervous system.**

50

51 Elucidating the origin and evolutionary history of life relies on the accurate placing of organisms,
52 extant and extinct, on the tree of life. This has historically been based upon anatomical similarities,
53 with clades being identified by shared derived characteristics (synapomorphies) that can be traced
54 to a most recent common ancestor and are not present in more distant groups and ancestors. For
55 extant organisms, such phylogenetic/cladistic classifications were revolutionised by molecular
56 biology, which utilizes differences and similarities in genetic sequences, predominately DNA and
57 RNA, to build trees of evolutionary relationships. However, despite being successfully applied to
58 recently extinct animals such as the giant moas from New Zealand^{1,2} or the iconic mammoth^{3,4},
59 these methods are of limited use for most fossil organisms, because observed rates of DNA
60 degradation indicate that in samples older than 1.5 million years, DNA is either severely crosslinked
61 or non-detectable⁵ and the oldest ancient DNA ever extracted (from permafrost-preserved
62 mammoth teeth) is 1.6 million years old⁴. Palaeontology has undergone its own revolution with the
63 advent of 3D X-ray microtomography and more recently a series of advanced 2D imaging
64 techniques, which reveal previously inaccessible or invisible anatomical information⁶⁻¹². These
65 techniques allow fossil anatomy to be described better than ever before, providing a wide range of
66 new characters that have led to better resolution of phylogenetic analyses¹³⁻¹⁵. Furthermore,
67 although DNA is not preserved in ancient fossils, remnants or derivatives of ancient biomolecules
68 can survive in the geological record, associated to organically-preserved fossil remains or isolated
69 within sedimentary rocks¹⁶⁻²⁶. Some of these compounds represent biomolecular signatures (or
70 “biomarkers”) diagnostic of particular (often broad) clades of organisms, and therefore represent a
71 powerful complement to fossil anatomies in revealing the history of life²⁰. Nonetheless, such
72 approaches provide little new information when applied to the majority of fossils whose
73 morphology and chemistry have substantially been altered during decay, burial, diagenesis and
74 weathering. As a result, recent studies focus on relatively “unaltered” specimens while many other
75 fossils remain enigmatic in their affinities. New tools and approaches accounting for and exploiting
76 information loss/gain during the taphonomic history are needed to help deciphering the affinities of
77 altered fossils^{20,27,28}.

78 Here we report the major-to-trace elemental composition of 14 strongly weathered fossil
79 animals, including various arthropods, annelids, sponges and an echinoderm, from the Early
80 Ordovician (Tremadocian) Fezouata Shale of Morocco^{29,30} using synchrotron-based X-ray
81 fluorescence (XRF) mapping. In this Burgess Shale-type deposit, fossils were originally preserved
82 as carbonaceous compressions and/or in authigenic minerals including pyrite^{31,32}, before being
83 extensively weathered by modern water circulations that led to the leaching of carbon from
84 carbonaceous compressions, the oxidation of pyrite crystals into yellow, red to purple iron oxide

85 pseudomorphs, the deposition of new, poorly crystallised Fe-oxides in previously non-pyritised
86 areas, and the dissolution of carbonates from the matrix and from the skeletal elements of animals
87 such as echinoderms^{31–34}. We consistently extracted mean XRF spectra from the tissues preserved
88 in our fossils, as well as from their surrounding sedimentary matrix (see Figs. 1A–M, Table S1 and
89 Figs. S1–S14 for location and details on the specimens and the selected areas, and methods for the
90 XRF spectra extraction strategy). Linear discriminant analysis (LDA) was then applied to assess
91 systematic variation in the major-to-trace elemental chemistry of different structure types (defined
92 according to Saleh et al.³⁵), i.e. between biomineralised, sclerotised, cuticularised, and internal
93 tissues, and the sedimentary matrix. We further show the potential of this framework to interpret the
94 anatomy of a highly weathered enigmatic organism from the Fezouata Biota.

95

96

97 **Results and Discussion**

98

99 **Highly weathered fossils preserve tissue-specific trace elemental chemistries.**

100 Our results show that although the fossils have all been extensively weathered to Fe-oxides (usually
101 goethite, more rarely hematite, as determined by Raman spectroscopy), their biomineralised,
102 sclerotised, cuticularised, and internal tissues can still be distinguished based on their trace element
103 composition (Fig. 1N). Iron is naturally the main element composing the fossils (as Fe-
104 oxyhydroxides), but it is also the main element probed by our analyses for the surrounding shale (as
105 Fe-bearing clay minerals) because light elements and particularly silicon cannot be detected with
106 the used setup (see Methods). All fossil tissues are, nevertheless, richer in Fe than the shale, and are
107 also considerably enriched in As and Pb (Fig. 1O). The proximity of biomineralised and sclerotised
108 tissues in the LDA plot indicates they have a similar elemental composition, only discriminated by a
109 slight enrichment in Ti and Zn in biomineralised tissues, and in Fe, Cu, As and Pb in sclerotised
110 tissues. Cuticularised tissues differ by strong depletions in Cu and As, as well as in Rb, Sr and Y.
111 The only internal tissue available for study contains little to no Ni, Cu, Zn and Ga, and is the most
112 depleted in Rb, Sr and Y. Note that no chemical inventory was collected for soft cellular outer
113 tissues in direct contact with seawater (e.g. tentacles) as they were never found preserved in the
114 Fezouata Biota^{32,35}.

115

116

117

118

The specific chemical inventory for each type of tissues can be further confirmed
considering that analysed fossils were found in numerous and distant (up to >30 km; Fig. S15)
contemporaneous outcrops with different modern-weathering history³¹. This means that the
chemical discrimination between different tissue types is not specific to a particular outcrop, and

119 tissue types can be chemically differentiated within the entire Fezouata Shale, because it was
120 affected by broadly similar water circulation processes in the Draa valley³². The high concentrations
121 and chemical speciation of the accessory metals imply that they have accumulated mainly through
122 reactive transport during diagenesis –before the material reaches a stage of depercolation where the
123 formation of specific fluid pathways and remineralisation blocks further uptake– rather than being
124 originally present in the living organism (and persisting through geological times). Indeed, Cu, As,
125 Pb, Ti and Zn concentrations in the 0.02–0.86 wt% range (see Table S2, and Methods for XRF
126 quantification) are exceeding by one to several orders of magnitude those encountered in modern
127 relatives of the Fezouata organisms, even when inhabiting environments heavily contaminated by
128 terrestrial pollutants^{37,38}. Furthermore, the most contrasting metal Cu is present in all investigated
129 fossils as a Cu-carbonate compound (Fig. S16), which ubiquitous occurrence in such a wide range
130 of organisms and tissues cannot be original, particularly considering that weathering led to the
131 dissolution of carbonates from skeletal elements of animals such as echinoderms^{31–34}. A description
132 of the precise mechanisms responsible for such a diagenetic uptake (i.e. percolation, deposition,
133 adsorption or substitution) is beyond the scope of the present work, but it clearly indicates that
134 tissue-specific physico-chemical differences persisted long enough after decay and early
135 mineralization to distinctly influence later elemental uptake, leading to elemental signatures that
136 were retained (at least locally) after extensive subsequent weathering.

137

138 **Trace elemental composition can identify tissue types in enigmatic fossils.**

139 Building on this tissue-specific chemical inventory, we used XRF mapping and the obtained LDA
140 classification to interpret the anatomy of an enigmatic, highly weathered organism (AA-FETB-OI-
141 22; Figs. 2A, B). While it is particularly challenging to optically investigate this specimen owing to
142 its poorly preserved state, the distributions of Fe (enriched in fossil tissues) (Fig. 2C) and to a larger
143 extent Rb (depleted in most fossil tissues) allow us to distinguish the outline of the organism (Fig.
144 2D), which does not include the entire brownish-purplish weathered surface. Chemically, we can
145 distinguish two different types of tissues in this fossil: one depleted in Rb (Fig. 2D), and a central,
146 3-mm wide tubular structure strongly enriched in Fe (Fig. 2C), optically yellowish and burgundy in
147 colour, which extends anteriorly into a 28-mm long, yellowish and unsegmented slender appendage
148 that curves along its length and tapers to a pointed end (Figs. 2B, C). We extracted mean XRF
149 spectra from these two tissues and the sedimentary matrix (see Fig. 2C, Table S1 and Fig. S17 for
150 location and details on the selected areas) and added them to our LDA classification (Fig. 2E). The
151 matrix spectrum perfectly clusters with the matrix spectra from the other Fezouata fossils. The
152 composition of the main body part clusters with that of cuticularised tissues. The anterior part of the

153 Fe-rich tubular structure, however, does not cluster with biomineralised, sclerotised or cuticularised
154 tissues. Its central position is in proximity to the one data point from known internal tissue, making
155 this the most likely tissue type for this tubular structure. The posterior part of this tubular structure,
156 which is more burgundy in colour (Fig. 2B) and of different trace elemental composition (richer in
157 Cu and Pb; Fig. 2F), plots distinctively from the anterior part, closer to the internal tissue point (Fig.
158 S17), and may therefore represent the remains of another internal system. Note that the richer in
159 iron the XRF spectra extracted from weathered matrix areas are the closer they plot to cuticularised
160 tissues, following the fact that the shale matrix (clay and silica) is way less concentrated in iron than
161 the fossil tissues (Fe-oxyhydroxides) (Fig. S17).

162 Using the elemental composition as a guide, a description of the overall anatomy of this
163 animal can be made (Fig. 2G). The organism has a cuticularised, 11-mm wide, elongated and
164 parallel-side trunk region, through which runs a central 3-mm wide band of internal tissues that
165 extends into a 28-mm long slender, tapering and unsegmented appendage. The trunk region shows
166 several faint discontinuous parallel lines that suggest the body was segmented and divided into a
167 minimum of 6 body units. Laterally to the trunk outline, the cuticularised tissues extend outwards
168 into poorly-defined wide lateral flaps that are rounded or roughly triangular in outline. This
169 combination of anatomical features is very reminiscent of *Kerygmachela kierkegaardii*, a stem-
170 group euarthropod from the Cambrian Sirius Passet Biota of Greenland^{39,40}. An affinity for the
171 Fezouata Shale organism similar to *K. kierkegaardii* would suggest that one of the pair of frontal
172 appendages has not been preserved in the Fezouata organism, explaining the asymmetrical position
173 of the one that is present. Regardless, due to the 40 Myr gap between the Sirius Passet and the
174 Fezouata Shale, it is unlikely that the Fezouata organism belongs to the same taxon. In any case,
175 stem euarthropod affinities for this organism increase the species richness of the Fezouata Biota.

176 A closer look at the regions of the specimen interpreted as internal tissues reveals anatomical
177 detail that allows us to identify the organ systems that are present. Microscopic examination of the
178 anterior yellowish region of the internal tissues reveals the presence, besides numerous rock
179 fractures, of lateral extensions (Fig. 3A). A higher-resolution XRF map (25- μ m pixel size) further
180 unveils four Fe-rich spherical structures organised antero-posteriorly, as well as another pair of two
181 spherical structures, not as rich in Fe, positioned laterally to the first spherical structure and
182 connected to it by an elbow duct (Figs. 3B,C). The only interpretation for such an arrangement of
183 structures is that they represent four ganglia of the nervous system and a pair of lateral eyes,
184 respectively (Fig. 3C,D). Although rare, the fossilisation of nervous tissues is being documented in
185 a growing number of fossils⁴⁰⁻⁴⁹. It is explained by the presence of highly reactive biogenic Fe in
186 the nervous system, which has been proposed to initiate selective pyritisation very rapidly during

187 early diagenesis while other tissues are still decaying⁵⁰. Nonetheless, the undisputable identification
188 of fossilised internal anatomical features as remains of nervous tissues may be challenging. Aria et
189 al. proposed a set of criteria for their recognition, namely the consideration of the specimen
190 topology, the morphoanatomical consistency, the taphonomic context and redundancy⁵¹. The
191 remains observed in AA-FETB-OI-22 meet most of the proposed criteria: surface relief has been
192 carefully considered, as shown in our interpretative drawing (Fig. 3C), especially as the Fe
193 distribution probed by XRF is not limited to the surface (see Methods) allowing us to confidently
194 distinguish between relief and fossilised remains; features are consistent with those described from
195 closely-related fossils⁴⁰; detailed knowledge of the taphonomy at the site³¹⁻³⁵ and the dorso-ventral
196 plane of preservation associated with some 3D preservation uncovered by XRF ensure that
197 taphonomic variations have been considered. We, however, acknowledge that the redundancy
198 criterion is not met, but we argue that if our method could uncover such new features in a random
199 specimen then more are expected to be discovered. The internal anatomical features preserved in
200 the analysed specimen therefore represent the first remains of a nervous system ever reported from
201 the Ordovician period. The other regions of the internal tubular structure that have a different
202 chemistry (Fig. 2F) likely represent remains of other internal tissues or systems (Fig. 2G).

203

204 **Towards a more exhaustive documentation of the history of life**

205 The identification, based upon the tissue-specific incorporation of inorganic minor and trace
206 elements, of a stem euarthropod yielding remains of the nervous system from Fezouata extends both
207 its biodiversity and the range of tissues that could be preserved there. It also illustrates the potential
208 of novel uses of advanced spectro-imaging techniques to identify pivotal yet poorly preserved
209 and/or highly weathered fossils such as lower stem euarthropods, which are neither biomineralised
210 nor sclerotised and as such have a low fossilisation potential.

211 Tissue-specific chemistry is known to be a powerful tool for interpreting the soft tissue
212 anatomy of exceptionally preserved fossils. This approach has been developed with XRF mapping
213 of a wide range of vertebrates retaining organometallic compounds derived from the original
214 melanin pigments⁵²⁻⁵⁴. Recently, the discovery that tissue-specific chemical signatures can persist in
215 fossilised internal melanosomes (quite common in the fossil record) has even suggested that it could
216 potentially be used to constrain the affinities of enigmatic fossil vertebrates⁵⁵. Yet, such an approach
217 is limited to literally exceptionally preserved fossils, i.e. retaining molecular and/or organelles
218 remains, which have only been affected by limited diagenetic⁵⁵⁻⁵⁷. In the case of most other fossils,
219 which only preserve hard parts (bones, shells, plates, ossicles, biomineralised cuticle), and
220 occasionally soft parts replicated in minerals during fossilisation and/or, diagenesis, the use of XRF

221 mapping has been limited to acquiring chemical information and visualising anatomical features
222 superficially hidden beneath the sample surface^{10,11,58-60}. Our study unexpectedly shows that the
223 combination of both the spatial and chemical information provided by elemental mapping with
224 appropriate sampling and data processing can represent, for a given locality, a powerful toolkit to
225 decipher the anatomy and affinities of poorly preserved and/or highly weathered soft-bodied fossils.
226 Documenting new anatomical features completes our knowledge of past biodiversity and ecology,
227 while uncovering hidden evolutionary patterns. As such, this approach holds great promise in
228 allowing a detailed understanding of overlooked aspects of the history of life.

229

230

231 **Materials and Methods**

232 **Fossil specimens.** The studied material is housed in the collections of the Musée cantonal de
233 Géologie de Lausanne (MGL), and of the Cadi-Ayyad University (Faculté des Sciences et
234 Techniques, Guéliz), Marrakesh, Morocco. The MGL material was collected by authorised and
235 academically recognised avocational Moroccan collector Mohamed Ben Moula and his family over
236 the period of 2015 to 2016; A.C.D. worked in collaboration with them to collect the metadata
237 associated with the collected fossils. Mohamed Ben Moula has a long-standing working relationship
238 with several academics, has received the Mary Anning Award from the Palaeontological
239 Association, and has a radiodont fossil named after him in honour of his great contribution to the
240 field of palaeontology. The collection was purchased with funds from the University of Lausanne
241 and the Swiss National Science Foundation, following all regulations for purchases. The material
242 was transported to Casablanca and subjected to export approval by the Ministry of Energy, Mines
243 and the Environment of the federal government of the Kingdom of Morocco and approved for
244 shipment to Switzerland on 11.05.2017 (export permits curated with the collection). The material
245 from the Marrakesh collection studied herein was loaned to the University Lyon 1 for study and will
246 be returned to the Cadi-Ayyad University after study.

247 Details about the fossil specimens investigated herein (identification, inventory numbers,
248 and localities) are given in Table S1. Precise locality information is curated with the specimens, and
249 available upon request from the authors. Specimens were selected to represent a variety of taxa and
250 tissue types, for which remains are thicker than 300 μm to make sure that the elemental signal
251 recorded using μXRF only comes from the fossil itself and not also from the underlying
252 sedimentary matrix. Details about the scanning steps and dwell times used for each map, as well as
253 about the areas from which spectra have been extracted are also given in Table S1.

254

255

256 **Elemental mapping.** Synchrotron micro X-ray fluorescence (μ XRF) major-to-trace elemental
257 mapping was performed at the DiffAbs beamline of the SOLEIL synchrotron source (France), using
258 a monochromatic beam of 18 keV ($\Delta E/E \sim 1-2 \times 10^{-4}$), selected for excitation of K-lines from
259 phosphorus to yttrium and L-lines from cadmium to uranium. In order to map the specimen with a
260 high lateral resolution, the beam was reduced down to a diameter of 50 μm using a molybdenum
261 pinhole. The sample was mounted on a scanner stage allowing 90 mm movements (in both
262 horizontal and vertical directions) with micrometre accuracy, and orientated at 45° with respect to
263 the incident beam. XRF was collected using a 4-element silicon drift detector (SDD, Vortex ME4,
264 Hitachi High-Technologies Science America, Inc., total active area: 170 mm^2) oriented at 90° with
265 respect to the incident beam, in the horizontal plane¹¹ in order to minimize the elastic (Thompson)
266 scattering signal.

267 Two-dimensional spectral images, *i.e.* images for which each pixel is characterised by a full
268 XRF spectrum, were collected *on the fly*⁶¹ over the specimens at a 20–200 μm lateral resolution
269 with a 20–70 ms dwell time (effective counting time was 90% of the dwell time) depending on the
270 samples (see Table S1 for the precise scanning steps and dwell times used for each map). Spectra
271 were then reduced by summing intensities from the four elements of the XRF detector, and
272 integrating intensities every 100 eV. All elemental distributions presented herein correspond to
273 integrated intensities from the main XRF peaks, produced using ImageJ and represented using grey,
274 RGB composite or Green Fire Blue colour scales.

275

276 **XRF spectra extraction.** Based on the obtained elemental distributions, we consistently extracted
277 mean XRF spectra from the different tissues preserved in our fossils, as well as from their
278 surrounding sedimentary matrix, carefully selecting homogeneous areas (see Figs. 1A–M, Table S1
279 and Figs. S1–S14 for location and details on the specimens and the selected areas). We particularly
280 avoided Mn-rich areas that resulted from recent weathering and covered parts of some fossils (Figs.
281 1D, G and L) as they would obscure other chemical signals; weathering in the Fezouata Shale was
282 also responsible for the leaching of carbon, oxidation of pyrite, deposition of Fe-oxides and
283 dissolution of carbonates^{31–34}. To compensate for the use of different exposure times between
284 datasets, the number of pixels for each area was adapted such that the collection time (and
285 consequently the signal-to-noise ratio) was similar between all extracted spectra (see Table S1).
286 Another important parameter to consider is the thickness of the fossil material. At 18 keV, the
287 attenuation length for goethite (the main iron oxyhydroxide in the Fezouata fossils) is about 80 μm :
288 it is therefore essential that extracted spectra are collected from fossil tissues thicker than this

289 length, so that the extracted signal is not the sum of contributions from the fossil and the underlying
290 sediment.

291

292 **Linear discriminant analyses.** Differences in elemental abundances between the tissue types of the
293 14 identified fossils were assessed using a linear discriminant analysis (LDA), a method that
294 explains (and predicts) the affiliation of an individual to a predefined class (group) based on the
295 measured predictive variable characteristics. The analyses were performed in the R statistical
296 environment using the `MASS` package⁶², and plotted using the `ggplot2` package⁶³. The statistical
297 analysis is based on the integrated intensity of the XRF signals of the different elements, with
298 partial reabsorption by the matrix. To discriminate between tissues, we directly rely on the fact that
299 the signal results from the statistical realisation of the photon-matter interaction (rather than
300 quantitative estimates). Discrimination therefore takes into account both the average content in each
301 element and its local distribution within each probed voxel (containing material of varying
302 composition). Prior to the LDA, bending followed by a rubberband baseline corrections were
303 applied to the log-normalised spectra using the `wl.eval` and `spc.rubberband` function of the
304 `hyperSpec` package⁶⁴. Spectra from the enigmatic organism were then added to the LDA plot
305 using the `predict` function. Spectra and the R script used in this work are available via the
306 following Dryad Digital Repository:

307 https://datadryad.org/stash/share/LGEGhXAwq2FZjiD12k9MPFfZ1D0Vt0Z_M1wLWXSKzSw
308 (private, randomized URL for Peer Review until the related manuscript has been accepted).

309

310 **XRF quantification.** Full quantification of trace elements from XRF maps of heterogeneous
311 materials such as fossils is generally hampered by local heterogeneity (both laterally and in depth),
312 which limits the precision of corrections for matrix X-ray reabsorption, with strong impact on the
313 calculated concentrations depending on the hypothesis on the matrix composition. Nonetheless, by
314 carefully selecting homogeneous areas (based on elemental distributions) and defining the matrix,
315 statistics are sufficient to estimate semi-quantitative contents of trace elements in fossils^{65,66}. We
316 estimated elemental concentrations in our fossils from a full spectral decomposition performed with
317 the PyMCA data analysis software⁶⁷ using an Hypermet peak shape, a polynomial approximation of
318 the baseline and experimental parameters, applying reabsorption corrections considering a goethite
319 matrix (as determined by Raman spectroscopy). The photon flux was estimated to 3.4×10^9
320 photons \cdot s⁻¹ taking Fe as internal standard (62.85wt% in pure goethite). Resulting concentrations
321 expressed as wt% are presented in Table S2.

322

323 **Acknowledgments**

324 We are grateful to SOLEIL synchrotron for provision of beamtime, D. Thiaudière, and P. Joly for
325 assistance at the DiffAbs beamline, as well as B. Lefebvre and E. Robert for facilitating access to
326 the material from the Marrakesh collection, and G. Potin for help with the Musée cantonal de
327 Géologie de Lausanne collection. P.G., F.P.P., L.Lu. and this research were funded by the Swiss
328 National Science Foundation, grant number 205321_179084 entitled “Arthropod Evolution during
329 the Ordovician Radiation: Insights from the Fezouata Biota” and awarded to A.C.D. L.La. was
330 supported by the Center for Geosphere Dynamics (UNCE/SCI/006), and by the institutional support
331 RVO 67985831 of the Institute of Geology of the Czech Academy of Sciences. F.S. acknowledges
332 funding from the Faculty of Geosciences and Environment of the University of Lausanne.

333

334

335 **References**

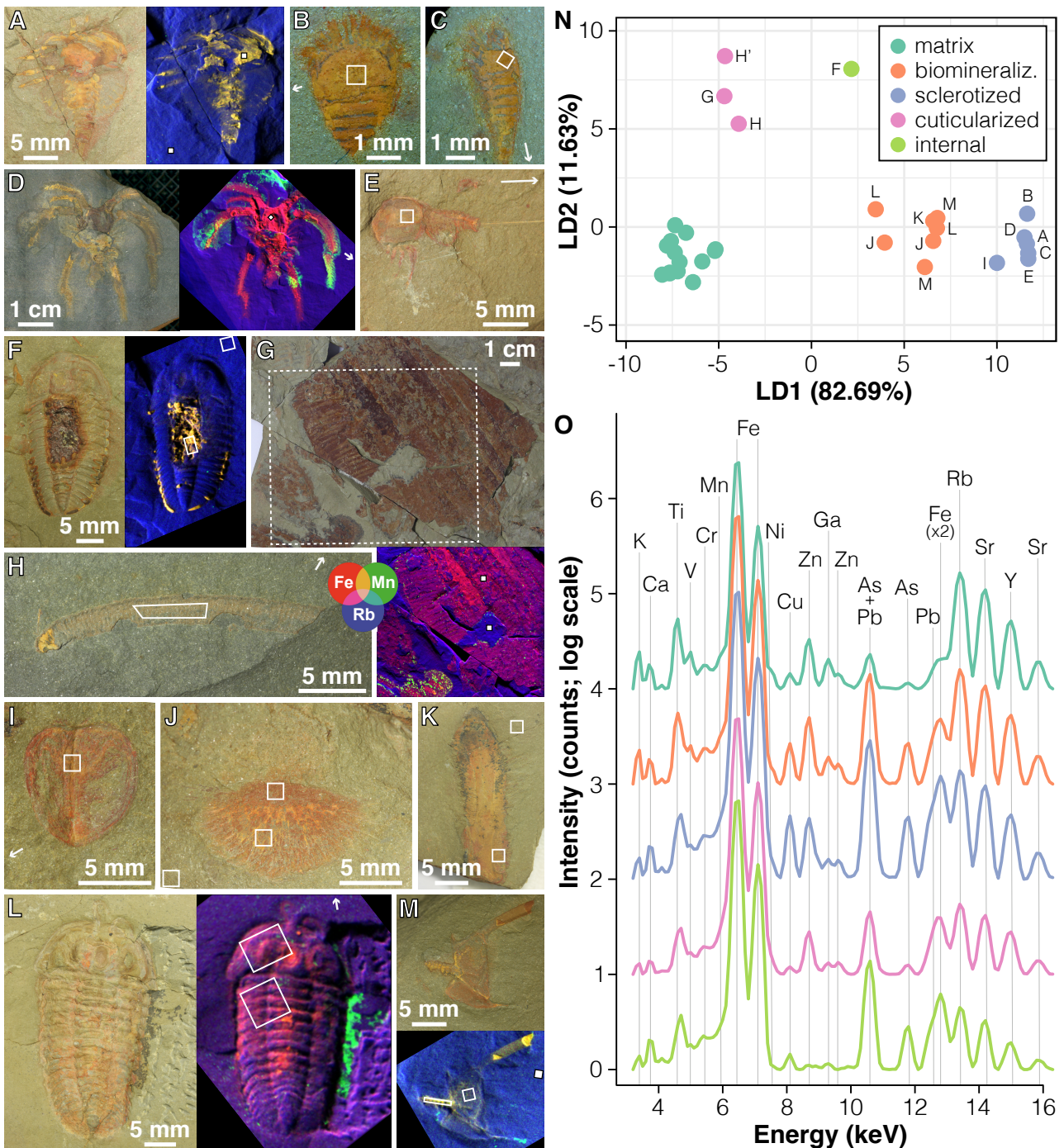
- 336 1. A. Cooper, C. Mourer-Chauviré, G. K. Chambers, A. von Haeseler, A. C. Wilson, S. Pääbo,
337 Independent origins of New Zealand moas and kiwis. *Proc. Natl. Acad. Sci. U.S.A.* **89**,
338 8741-8744 (1992).
- 339 2. A. J. Baker, L. J. Huynen, O. Haddrath, C. D. Millar, D. M. Lambert, Reconstructing the
340 tempo and mode of evolution in an extinct clade of birds with ancient DNA: the giant moas
341 of New Zealand. *Proc. Natl. Acad. Sci. U.S.A.* **102**, 8257-8262 (2005).
- 342 3. R. Debruyne, V. Barriel, P. Tassy, Mitochondrial cytochrome *b* of the Lyakhov mammoth
343 (Proboscidea, Mammalia): new data and phylogenetic analyses of Elephantidae. *Mol.*
344 *Phylogenet. Evol.* **26**, 421–434 (2003).
- 345 4. T. van der Valk, P. Pečnerová, D. Díez-del-Molino, A. Bergström, J. Oppenheimer *et al.*
346 Million-year-old DNA sheds light on the genomic history of mammoths. *Nature* **591**, 265–
347 269 (2021).
- 348 5. E. Willerslev, A. J. Hansen, R. Rønn, T. B. Brand, I. Barnes, C. Wiuf, D. Gilichinsky, D.
349 Mitchell, A. Cooper, Long-term persistence of bacterial DNA. *Curr. Biol.* **14**, R9–R10
350 (2004).
- 351 6. P. Tafforeau, R. Boistel, E. Boller, A. Bravin, M. Brunet *et al.*, Applications of X-ray
352 synchrotron microtomography for non-destructive 3D studies of paleontological specimens.
353 *Appl. Phys. A* **83**, 195–202 (2006).
- 354 7. S. Y. Smith, M. E. Collinson, P. J. Rudall, D. A. Simpson, F. Marone, M. Stampanoni,
355 Virtual taphonomy using synchrotron tomographic microscopy reveals cryptic features and
356 internal structure of modern and fossil plants. *Proc. Natl. Acad. Sci. U.S.A.* **106**, 12013-
357 12018 (2009).
- 358 8. U. Bergmann, R. W. Morton, P. L. Manning, W. I. Sellers, S. Farrar, K. G. Huntley, R. A.
359 Wogelius, P. L. Larson, *Archaeopteryx* feathers and bone chemistry fully revealed via
360 synchrotron imaging. *Proc. Natl. Acad. Sci. U.S.A.* **107**, 9060–9065 (2010).
- 361 9. U. Bergmann, L. Bertrand, N. P. Edwards, P. L. Manning, R. A. Wogelius, “Chemical
362 mapping of ancient artifacts and fossils with x-ray spectroscopy” in *Synchrotron Light*

- 363 *Sources and Free-Electron Lasers: Accelerator Physics, Instrumentation and Science*
364 *Applications*, E. Jaeschke, S. Khan, J. R. Schneider, J. B. Hastings, Eds. (Springer Nature
365 Switzerland, 2019).
- 366 10. P. Gueriau, C. Mocuta, D. B. Dutheil, S. X. Cohen, D. Thiaudière, The OT1 Consortium, S.
367 Charbonnier, G. Clément, L. Bertrand, Trace elemental imaging of rare earth elements
368 discriminates tissues at microscale in flat fossils. *PLoS One* **9**, e86946 (2014).
- 369 11. P. Gueriau, C. Jauvion, C. Mocuta, Show me your yttrium, and I will tell you who you are:
370 implications for fossil imaging. *Palaeontology* **61**, 981–990 (2018).
- 371 12. T. G. Kaye, A. R. Falk, M. Pittman, P. C. Sereno, L. D. Martin, D. A. Burnham, E. Gong, X.
372 Xu, Y. Wang, Laser-Stimulated Fluorescence in Paleontology. *PLoS One* **10**, e0125923
373 (2015).
- 374 13. S. Giles, M. Friedman, M. Brazeau, Osteichthyan-like cranial conditions in an Early
375 Devonian stem gnathostome. *Nature* **520**, 82–85 (2015).
- 376 14. D. Zhai, J. Ortega-Hernández, J. M. Wolfe, X. Hou, C. Cao, Y. Liu, Three-dimensionally
377 preserved appendages in an Early Cambrian stem-group pancrustacean. *Curr. Biol.* **29**, 171–
378 177 (2019).
- 379 15. T. Miyashita, M. I. Coates, R. Farrar, P. Larson, P. L. Manning, R. A. Wogelius, N. P.
380 Edwards, J. Anné, U. Bergmann, A. R. Palmer, P. J. Currie, Hagfish from the Cretaceous
381 Tethys Sea and a reconciliation of the morphological–molecular conflict in early vertebrate
382 phylogeny. *Proc. Natl. Acad. Sci. U.S.A.* **116**, 2146–2151 (2019).
- 383 16. J. J. Brocks, R. E. Summons, Sedimentary Hydrocarbons. *Biogeochemistry* **8**, 63–115
384 (2005).
- 385 17. J. J. Brocks, A. Pearson, Building the biomarker tree of life. *Rev. Mineral. Geochem.* **59**,
386 233–258 (2005).
- 387 18. J. Lindgren, P. Uvdal, P. Sjövall, D. E. Nilsson, A. Engdahl *et al.*, Molecular preservation of
388 the pigment melanin in fossil melanosomes. *Nat. Communications* **3**, 824 (2012).
- 389 19. D. E. Greenwalt, Y. S. Goreva, S. M. Siljeström, T. Rose, R. E. Harbach, Hemoglobin-
390 derived porphyrins preserved in a Middle Eocene blood-engorged mosquito. *Proc. Natl.*
391 *Acad. Sci. U.S.A.* **110**, 18496–18500 (2013).
- 392 20. D. E. G. Briggs, R. Summons, Ancient biomolecules: their origins, fossilization, and role in
393 revealing the history of life. *BioEssays* **36**, 482–490 (2014).
- 394 21. C. Colleary, A. Dolocan, J. Gardner, S. Singh, M. Wuttke *et al.*, Chemical, experimental,
395 and morphological evidence for diagenetically altered melanin in exceptionally preserved
396 fossils. *Proc. Natl. Acad. Sci. U.S.A.* **112**, 12592–12597 (2015).
- 397 22. Y. Pan, W. Zheng, A. E. Moyer, J. K. O’Connor, M. Wang *et al.*, Molecular evidence of
398 keratin and melanosomes in feathers of the Early Cretaceous bird *Eoconfuciusornis*. *Proc.*
399 *Natl. Acad. Sci. U.S.A.* **113**, E7900–E7907 (2016).
- 400 23. V. Vajda, M. Pucetaite, S. McLoughlin, A. Engdahl, J. Heimdal, P. Uvdal, Molecular
401 signatures of fossil leaves provide unexpected new evidence for extinct plant relationships.
402 *Nat. Ecol. Evol.* **1**, 1093–1099 (2017).
- 403 24. I. Bobrovskiy, J. M. Hope, A. Ivantsov, B. J. Nettersheim, C. Hallmann, J. J. Brocks,
404 Ancient steroids establish the Ediacaran fossil *Dickinsonia* as one of the earliest animals.
405 *Science* **361**, 1246–1249 (2018).

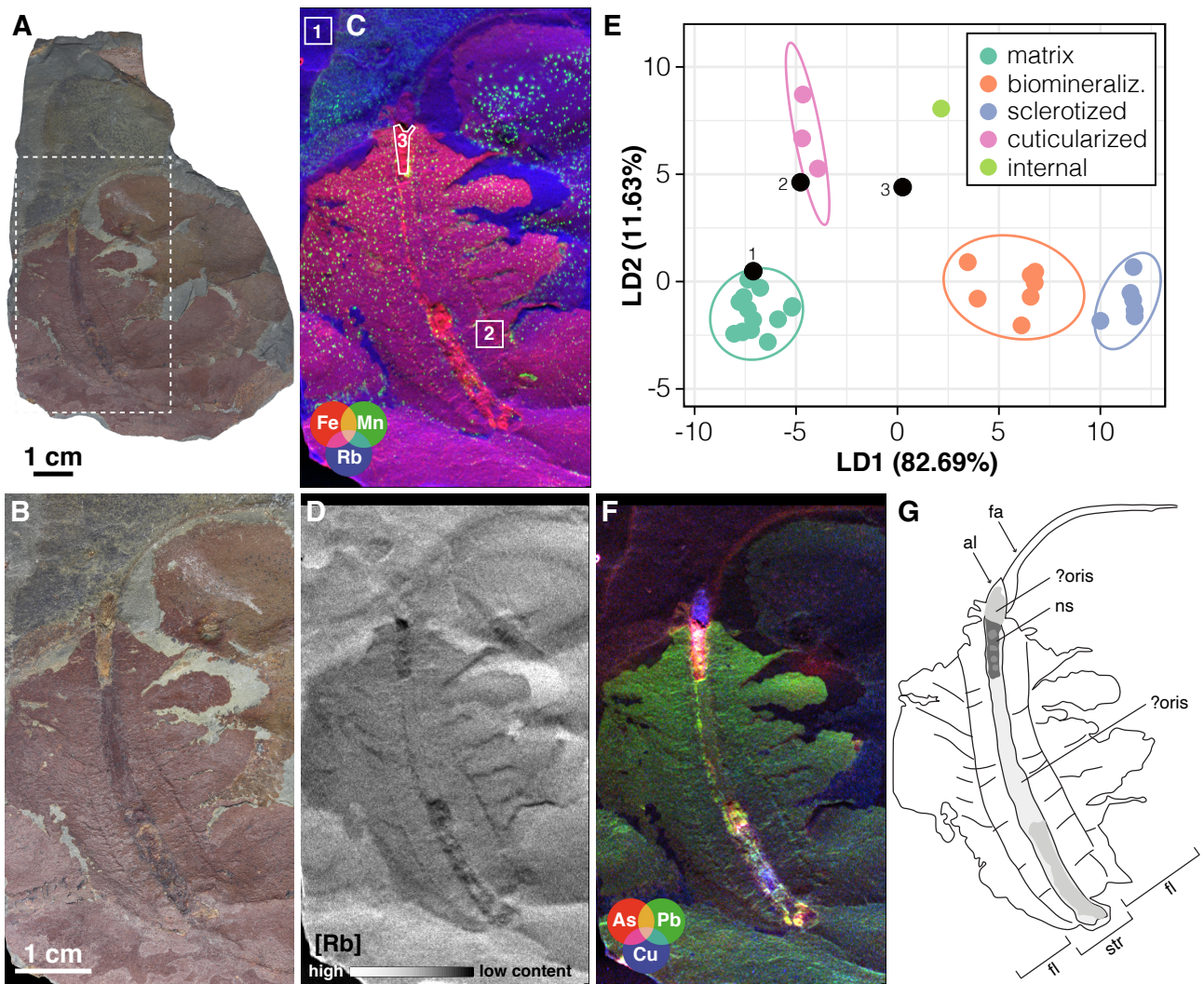
- 406 25. Y. Pan, W. Zheng, R. H. Sawyer, M. W. Pennington, X. Zheng *et al.*, The molecular
407 evolution of feathers with direct evidence from fossils. *Proc. Natl. Acad. Sci. U.S.A.* **116**,
408 3018–3023 (2019).
- 409 26. K. H. Kjær, M. Winther Pedersen, B. De Sanctis, B. De Cahsan, T. S. Korneliussen *et al.*, A
410 2-million-year-old ecosystem in Greenland uncovered by environmental DNA. *Nature* **612**,
411 283–291 (2022).
- 412 27. D. J. Murdock, S. E. Gabbott, M. A. Purnell M.A., The impact of taphonomic data on
413 phylogenetic resolution: *Helenodora inopinata* (Carboniferous, Mazon Creek Lagerstätte)
414 and the onychophoran stem lineage. *BMC Evol. Biol.* **16**, 19 (2016).
- 415 28. L. Bertrand, M. Thoury, P. Gueriau, É. Anheim, S. Cohen, Deciphering the Chemistry of
416 Cultural Heritage: Targeting Material Properties by Coupling Spectral Imaging with Image
417 Analysis. *Acc. Chem. Res.* **54**, 19670–19676 (2021).
- 418 29. P. Van Roy, P. J. Orr, J. P. Botting, L. A. Muir, J. Vinther, B. Lefebvre, K. El Hariri, D. E.
419 G. Briggs, Ordovician faunas of Burgess Shale type. *Nature* **465**, 215–218 (2010).
- 420 30. P. Van Roy, D. E. G. Briggs, R. R. Gaines, The Fezouata fossils of Morocco; an
421 extraordinary record of marine life in the Early Ordovician. *J. Geol. Soc.* **172**, 541–549
422 (2015).
- 423 31. F. Saleh, B. Pittet, P. Sansjofre, P. Gueriau, S. Lalonde *et al.*, Taphonomic pathway of
424 exceptionally preserved fossils in the Lower Ordovician of Morocco. *Geobios* **60**, 99–115
425 (2020).
- 426 32. F. Saleh, R. Vaucher, J. B. Antcliffé, A. C. Daley, K. El Hariri *et al.*, Insights into soft-part
427 preservation from the Early Ordovician Fezouata Biota. *Earth-Science Reviews* **213**, 103464
428 (2021).
- 429 33. B. Lefebvre, T. E. Guensburg, E. L. O. Martin, R. Mooi, E. Nardin *et al.*, Exceptionally
430 preserved soft parts in fossils from the Lower Ordovician of Morocco clarify stylophoran
431 affinities within basal deuterostomes. *Geobios* **52**, 27–36 (2019).
- 432 34. F. Saleh, B. Lefebvre, A. W. Hunter, M. Nohejlov, Fossil weathering and preparation mimic
433 soft tissues in eocrinoid and somasteroid echinoderms from the Lower Ordovician of
434 Morocco. *Microscopy today* **28**, 24–28 (2020).
- 435 35. F. Saleh, J. B. Antcliffé, B. Lefebvre, B. Pittet, L. Laibl *et al.*, Taphonomic bias in
436 exceptionally preserved biotas. *Earth and Planetary Science Letters* **529**, 115873 (2020).
- 437 36. P. Brouwer, *Theory of XRF* (PANalytical B.V., Almelo, The Netherlands, 2006).
- 438 37. J. Burger, C. Dixon, T. Shukla, N. Tsipoura, M. Gochfeld, Metal levels in horseshoe crabs
439 (*Limulus polyphemus*) from Maine to Florida. *Environmental research* **90**, 227–236 (2002).
- 440 38. Q. Liu, X. Xu, J. Zeng, X. Shi, Y. Liao *et al.*, Heavy metal concentrations in commercial
441 marine organisms from Xiangshan Bay, China, and the potential health risks. *Marine*
442 *pollution bulletin* **141**, 215–226 (2019).
- 443 39. G. B. Budd, A Cambrian gilled lobopod from Greenland. *Nature* **364**, 709–711 (1993).
- 444 40. T.-Y. S. Park, J.-H. Kihm, J. Woo, C. Park, W. Y. Lee, M. P. Smith, D. A. T. Harper, F.
445 Young, A. T. Nielsen, J. Vinther, Brain and eyes of *Kerygmachela* reveal protocerebral
446 ancestry of the panarthropod head. *Nature Communications* **9**, 1019 (2018).
- 447 41. X. Ma, X. Hou, G. D. Edgecombe, N. J. Strausfeld, Complex brain and optic lobes in an
448 early Cambrian arthropod. *Nature* **490**, 258–261 (2012).

- 449 42. G. Tanaka, X. Hou, X. Ma, G. D. Edgecombe, N. J. Strausfeld, Chelicerate neural ground
450 pattern in a Cambrian great appendage arthropod. *Nature* **502**, 364–367 (2013).
- 451 43. P. Cong, X. Ma, X. Hou, G. D., Edgecombe, N. J. Strausfeld, Brain structure resolves the
452 segmental affinity of anomalocaridid appendages. *Nature* **513**, 538–542 (2014).
- 453 44. J. Yang, J. Ortega-Hernández, N. J. Butterfield, Y. Liu, G. S. Boyan, J.-b. Hou, T. Lan, X.-g.
454 Zhang, Fuxianhuiid ventral nerve cord and early nervous system evolution in
455 Panarthropoda. *Proc. Natl. Acad. Sci. U.S.A.* **113**, 2988–2993 (2016).
- 456 45. L. Parry, J. B. Caron, *Canadia spinosa* and the early evolution of the annelid nervous
457 system. *Science advances* **5**, eaax5858 (2019).
- 458 46. T. Lan, Y. Zhao, F. Zhao, Y. He, P. Martinez, N. J. Strausfeld, Leanchoiliidae reveals the
459 ancestral organization of the stem euarthropod brain. *Current Biology* **31**, 4397–4404
460 (2021).
- 461 47. J. Ortega-Hernández, R. Lerosey-Aubril, S. R. Losso, J. C. Weaver, Neuroanatomy in a
462 middle Cambrian mollisoniid and the ancestral nervous system organization of chelicerates.
463 *Nature communications* **13**, 410 (2022).
- 464 48. N. J. Strausfeld, X. Hou, M. E. Sayre, F. Hirth, The lower Cambrian lobopodian
465 *Cardiodictyon* resolves the origin of euarthropod brains. *Science* **378**, 905–909 (2022).
- 466 49. R. T. Figueroa, D. Goodvin, M. A. Kolmann, M. I. Coates, A. M. Caron, M. Friedman, S.
467 Giles, Exceptional fossil preservation and evolution of the ray-finned fish brain. *Nature*
468 (2023). <https://doi.org/10.1038/s41586-022-05666-1>.
- 469 50. F. Saleh, A. C. Daley, B. Lefebvre, B. Pittet, J. P. Perrillat, Biogenic iron preserves
470 structures during fossilization: a hypothesis: iron from decaying tissues may stabilize their
471 morphology in the fossil record. *BioEssays* **42**, 1900243 (2020).
- 472 51. C. Aria, J. Vannier, J., T. Y. S. Park, R. R. Gaines, Interpreting fossilized nervous tissues.
473 *BioEssays* (2023). <https://doi.org/10.1002/bies.202200167>.
- 474 52. R. A. Wogelius, P. L. Manning, H. E. Barden, N. P. Edwards, S. M. Webb, W. I. Sellers, K.
475 G. Taylor, P. L. Larson, P. Dodson, H. You, L. Da-qing, U. Bergmann, Trace metals as
476 biomarkers for eumelanin pigment in the fossil record. *Science* **333**, 1622–1626 (2011).
- 477 53. V. M. Egerton, R. A. Wogelius, M. A., Norell, N. P. Edwards, W. I. Sellers, U. Bergmann,
478 D. Sokaras, R. Alonso-Mori, K. Ignatyev, A. van Veelen, J. Anné, B. E. van Dongen, F.
479 Knoll, P. L. Manning, The mapping and differentiation of biological and environmental
480 elemental signatures in the fossil remains of a 50 million year old bird. *Journal of Analytical*
481 *Atomic Spectrometry* **30**, 627–634 (2015).
- 482 54. P. L. Manning, N. P. Edwards, U. Bergmann, J. Anné, W. I. Sellers, A. van Veelen, D.
483 Sokaras, V. M. Egerton, R. Alonso-Mori, K. Ignatyev, B. E. van Dongen, K. Wakamatsu, S.
484 Ito, F. Knoll, R. A. Wogelius, Pheomelanin pigment remnants mapped in fossils of an
485 extinct mammal. *Nature Communications* **10**, 2250 (2019).
- 486 55. V. Rossi, M. E. McNamara, S. M. Webb, S. Ito, K. Wakamatsu, Tissue-specific geometry
487 and chemistry of modern and fossilized melanosomes reveal internal anatomy of extinct
488 vertebrates. *Proc. Natl. Acad. Sci. U.S.A.* **116**, 17880–17889 (2019).
- 489 56. V. Rossi, S. M. Webb, M. E. McNamara, Hierarchical biota-level and taxonomic controls on
490 the chemistry of fossil melanosomes revealed using synchrotron X-ray fluorescence.
491 *Scientific Reports* **10**, 8970 (2020).

- 492 57. V. Rossi, S. M. Webb, M. E. McNamara, Maturation experiments reveal bias in the
493 chemistry of fossil melanosomes. *Geology* **49**, 784–788 (2021).
- 494 58. A. Brayard, P. Gueriau, M. Thoury, G. Escarguel, the Paris Biota team, Glow in the dark:
495 Use of synchrotron μ XRF trace elemental mapping and multispectral macro-imaging on
496 fossils from the Paris Biota (Bear Lake County, Idaho, USA). *Geobios* **54**, 71–79 (2019).
- 497 59. T. Saucède, E. Vennin, E. Fara, N. Olivier, the Paris Biota team, A new holocrinid
498 (Articulata) from the Paris Biota (Bear Lake County, Idaho, USA) highlights the high
499 diversity of Early Triassic crinoids. *Geobios* **54**, 45–53 (2019).
- 500 60. P. Gueriau, J. C., Lamsdell, R. A. Wogelius, P. L. Manning, V. M. Egerton, U. Bergmann,
501 L. Bertrand, J. Denayer, A new Devonian euthycarcinoid evidences the use of different
502 respiratory strategies during the marine-to-terrestrial transition in the myriapod lineage.
503 *Royal Society Open Science* **7**, 201037 (2020).
- 504 61. N. Leclercq, J. Berthault, F. Langlois, S. Le, S. Poirier, J. Bisou, F. Blache, K. Medjoubi, C
505 Mocuta, Flyscan: a fast and multi-technique data acquisition platform for the SOLEIL
506 beamlines. *ICALPCS 2015, the 15th International Conference on Accelerator and Large
507 Experimental Control Systems*, 17–23 October 2015, Melbourne, Australia, Abstract No.
508 WEPGF056 (2015).
- 509 62. W. N. Venables, B. D. Ripley, *Modern Applied Statistics with S* (Springer-Verlag New
510 York, 2002).
- 511 63. H. Wickham, *ggplot2: Elegant Graphics for Data Analysis* (Springer-Verlag New York,
512 2016).
- 513 64. C. Beleites, V. Sergo, hyperSpec: a package to handle hyperspectral data sets in R, *R
514 package version 0.99-20201127*. (<https://github.com/cbeleites/hyperSpec>) (2020).
- 515 65. P. Gueriau, C. Mocuta, L. Bertrand, Cerium anomaly at microscale in fossils. *Analytical
516 Chemistry* **87**, 8827–8836 (2015).
- 517 66. P. Gueriau, S. Bernard, F. Farges, C. Mocuta, D. B. Dutheil *et al.*, Oxidative conditions can
518 lead to exceptional preservation through phosphatization. *Geology* **48**, 1164–1168 (2020).
- 519 67. V. A. Solé, E. Papillon, M. Cotte, P. Walter, J. Susini, A multiplatform code for the analysis
520 of energy-dispersive X-ray fluorescence spectra. *Spectrochimica Acta Part B: Atomic
521 Spectroscopy* **62**, 63–68 (2007).
- 522



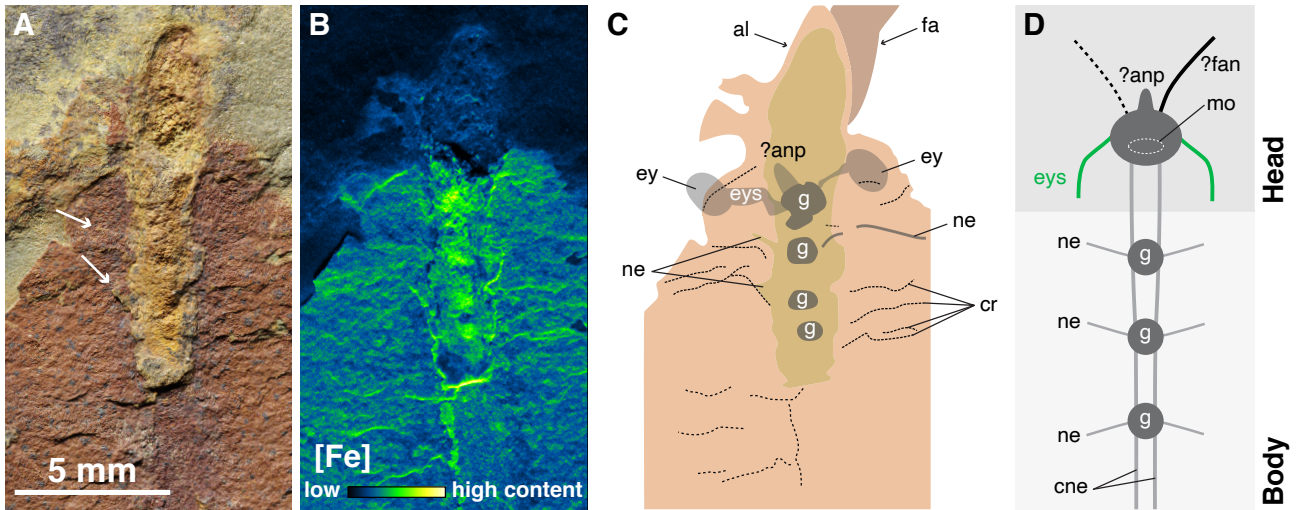
523
 524 **Figure 1. Synchrotron-based XRF major-to-trace elemental mapping of 14 fossil animals from**
 525 **the Early Ordovician Fezouata Shale of Morocco.** (A–M) Optical photograph and false-colour
 526 overlays of iron (red), manganese (green), and rubidium (blue) distributions of the analysed fossils
 527 (see Table S1 for specimen details and acquisition parameters). (N) Linear discriminant analysis of
 528 the mean XRF spectra extracted from the white box areas in A–M; white arrows locate spectra for
 529 the shale matrix that were taken outside of the displayed field of view, their length being
 530 proportional to the distance from the sampled area (see Figs. S1–S14 for precise locations). (O)
 531 Mean XRF spectrum for each tissue type and the matrix, vertically shifted for readability. The
 532 ‘Fe ×2’ peak in the fossil spectra corresponds to a Fe pile-up peak, an artefactual peak³⁶ that
 533 increases with concentration and further indicate that fossil tissues are richer in Fe than the shale.
 534 **[planned for 2-column width]**



535
 536 **Figure 2. Synchrotron-based XRF major-to-trace elemental mapping of a highly weathered**
 537 **organism (AA-FETB-OI-22) from the Early Ordovician Fezouata Shale of Morocco.** (A)
 538 Optical photograph of the entire slab. (B) Close-up on the specimen, from the dotted white box area
 539 in A. (C) False-colour overlay of iron (red), manganese (green), and rubidium (blue) distributions
 540 from the area in B. Acquisition parameters: 100×100 μm² scan step, 20 ms dwell time, 215 280
 541 pixels. Numbered white box areas indicate location of XRF spectra in E. (D) Rubidium distribution
 542 only. (E) Classification of the mean XRF spectra extracted from the white box areas in C within our
 543 LDA. (F) False-colour overlay of arsenic (red), lead (green), and copper (blue) distributions. (G)
 544 Interpretative line drawing of the anatomy of the specimen. Abbreviations: al, anterior lobe; fa,
 545 frontal appendage; fl, lateral flaps; ns, nervous system; ?oris, other remains of internal system(s);
 546 str, segmented trunk.

547 **[planned for 2-column width]**

548



549
 550 **Figure 3. Remains of the nervous system in AA-FETB-OI-22.** (A) Close-up optical photograph
 551 of the head and anteriormost portion of the body. Arrows highlight lateral extensions of the
 552 yellowish region. (B) Iron distribution (XRF contrast map). Acquisition parameters: $25 \times 25 \mu\text{m}^2$
 553 scan step, 20 ms dwell time, 264 163 pixels. (C) Interpretative line drawing. (D) Schematic
 554 reconstructed of the nervous system. Abbreviations: al, anterior lobe; anp, anterior neural
 555 projection, cne, central nerves, cr, cracks; ey, eye; eys, eye stalk; g, ganglion; fa, frontal appendage;
 556 fan, frontal appendage nerves; mo, mouth; ne, nerves.

557 **[planned for 2-column width]**

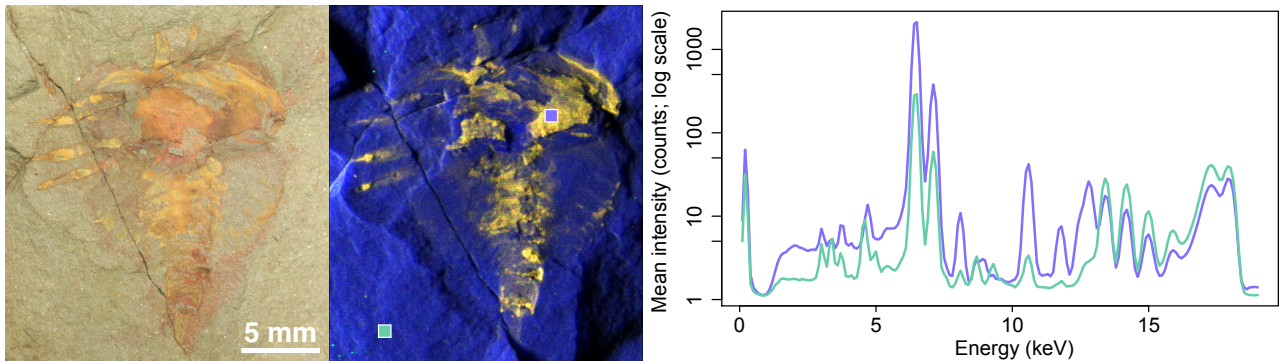
558

559

560 **Extended Data Figures.**

561

562



563

564

565

566

567

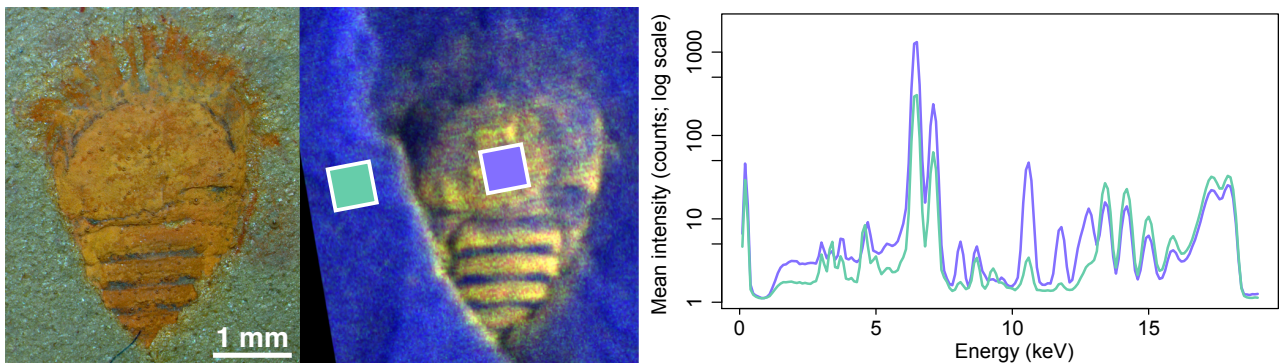
568

569

570

571

Figure S1. Synchrotron-based XRF major-to-trace elemental mapping of MGL 102701, an undescribed “xiphosuran” from the Early Ordovician Fezouata Shale of Morocco. Optical photograph (*left*), false-colour overlays of iron (red), manganese (green), and rubidium (blue) distributions (*centre*), and the extracted mean XRF spectra from box areas of corresponding colours in the elemental overlay (*right*). Refer to Fig. 1O for peak identification.



572

573

574

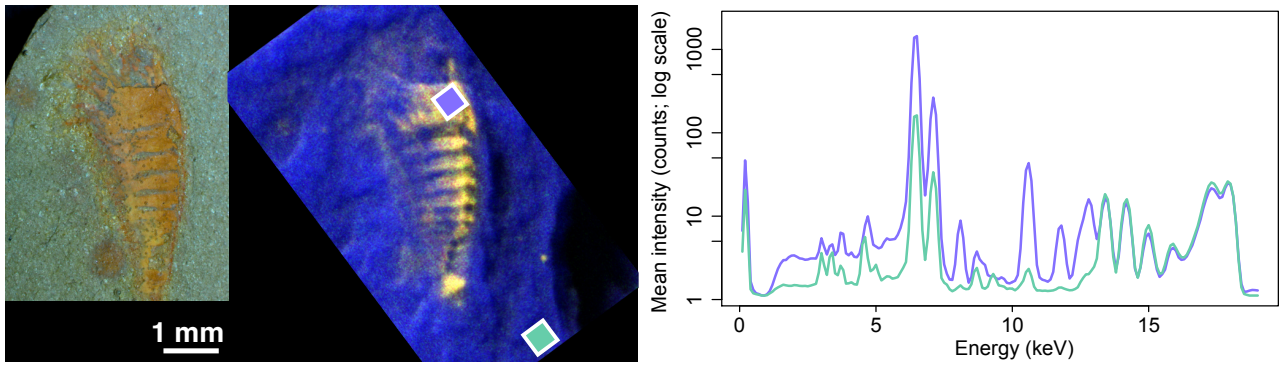
575

576

577

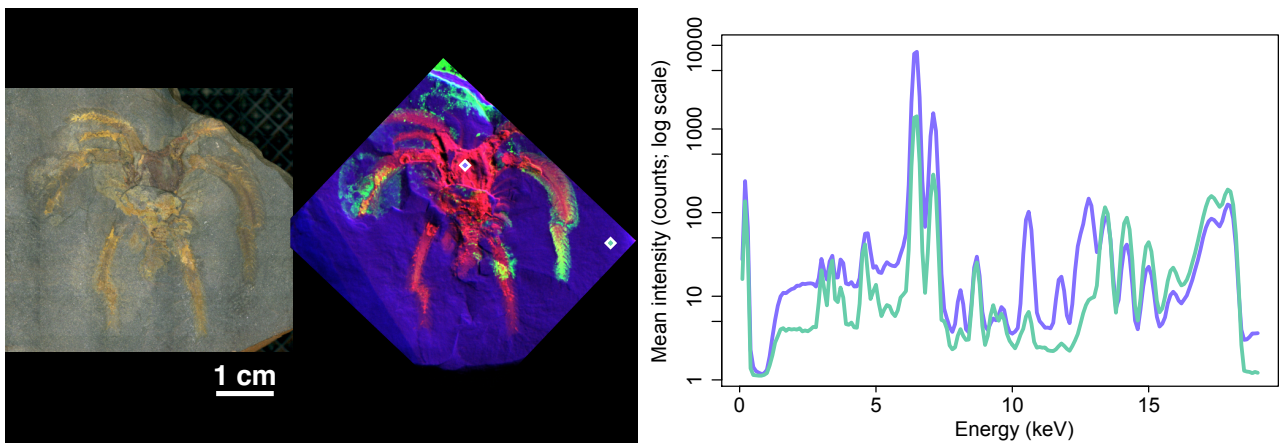
578

Figure S2. Synchrotron-based XRF major-to-trace elemental mapping of MGL 107210, an undescribed “synziphosurine” from the Early Ordovician Fezouata Shale of Morocco. Optical photograph (*left*), false-colour overlays of iron (red), manganese (green), and rubidium (blue) distributions (*centre*), and the extracted mean XRF spectra from box areas of corresponding colours in the elemental overlay (*right*). Refer to Fig. 1O for peak identification.



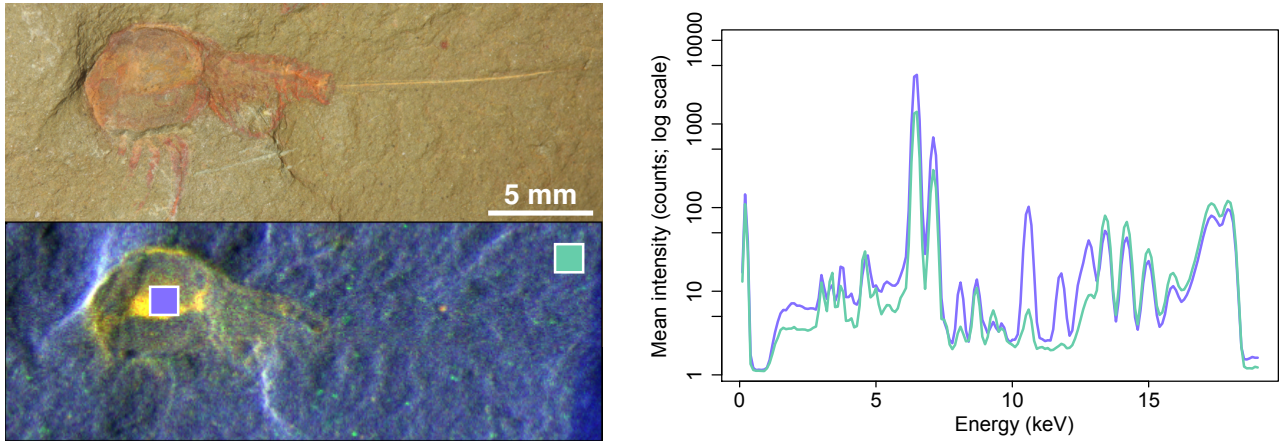
579
580
581
582
583
584
585
586
587
588

Figure S3. Synchrotron-based XRF major-to-trace elemental mapping of MGL 102841, an undescribed "synziphosurine" from the Early Ordovician Fezouata Shale of Morocco. Optical photograph (*left*), false-colour overlays of iron (red), manganese (green), and rubidium (blue) distributions (*centre*), and the extracted mean XRF spectra from box areas of corresponding colours in the elemental overlay (*right*). Refer to Fig. 1O for peak identification.



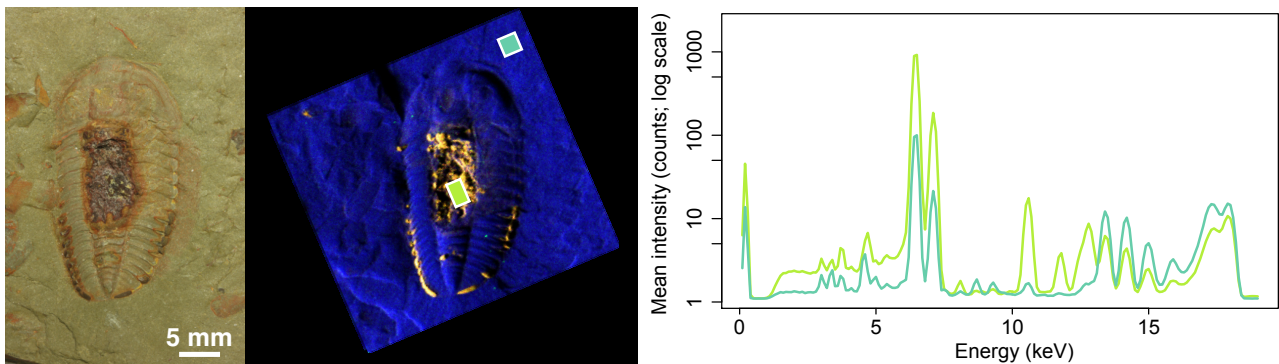
589
590
591
592
593
594
595

Figure S4. Synchrotron-based XRF major-to-trace elemental mapping of AA-BIZ31-OI-39, an undescribed "marrellid" from the Early Ordovician Fezouata Shale of Morocco. Optical photograph (*left*), false-colour overlays of iron (red), manganese (green), and rubidium (blue) distributions (*centre*), and the extracted mean XRF spectra from box areas of corresponding colours in the elemental overlay (*right*). Refer to Fig. 1O for peak identification.



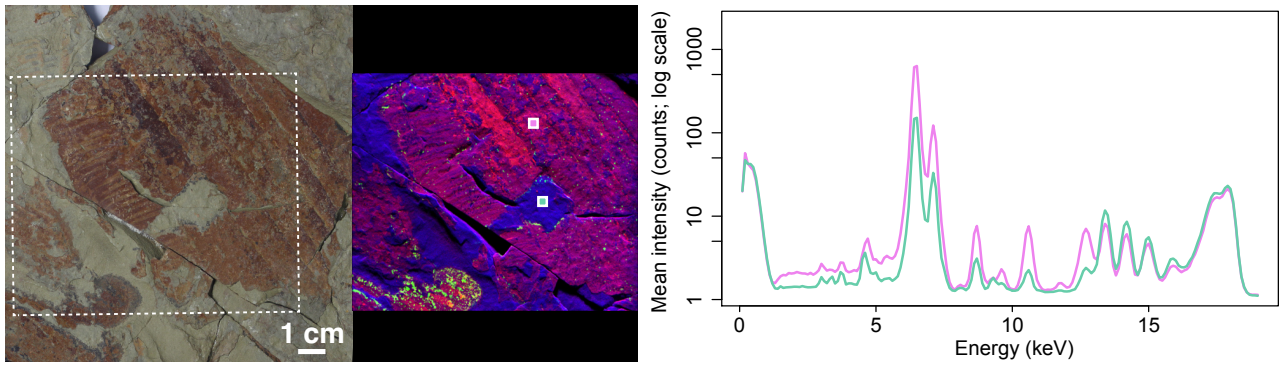
596
 597 **Figure S5. Synchrotron-based XRF major-to-trace elemental mapping of MGL 102705, an**
 598 **undescribed “xiphosuran” from the Early Ordovician Fezouata Shale of Morocco.** Optical
 599 photograph (*top left*), false-colour overlays of iron (red), manganese (green), and rubidium (blue)
 600 distributions (*bottom left*), and the extracted mean XRF spectra from box areas of corresponding
 601 colours in the elemental overlay (*right*). Refer to Fig. 1O for peak identification.

602
 603
 604
 605



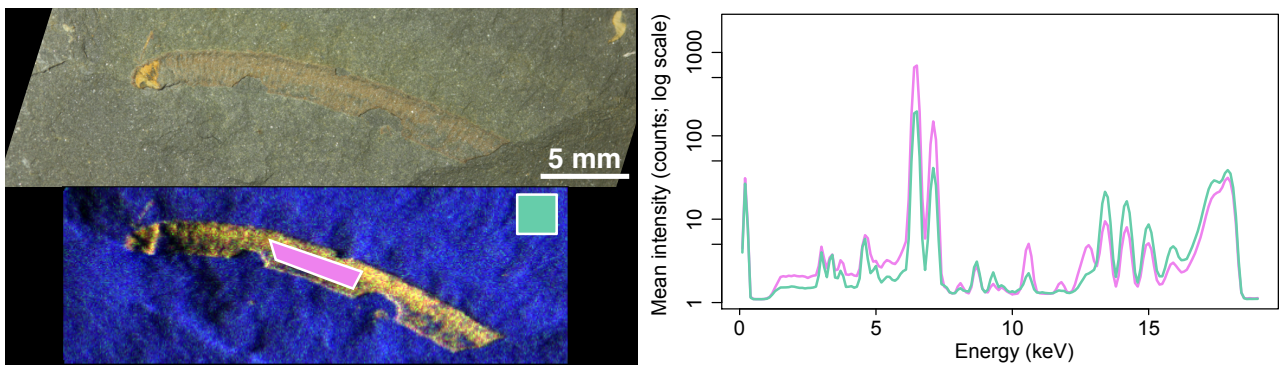
606
 607 **Figure S6. Synchrotron-based XRF major-to-trace elemental mapping of the trilobite**
 608 ***Bavarilla zemmourensis* Destombes, Sougy & Willefert, 1969, specimen MGL 102177, from the**
 609 **Early Ordovician Fezouata Shale of Morocco.** Optical photograph (*left*), false-colour overlays of
 610 iron (red), manganese (green), and rubidium (blue) distributions (*centre*), and the extracted mean
 611 XRF spectra from box areas of corresponding colours in the elemental overlay (*right*). Refer to Fig.
 612 1O for peak identification.

613



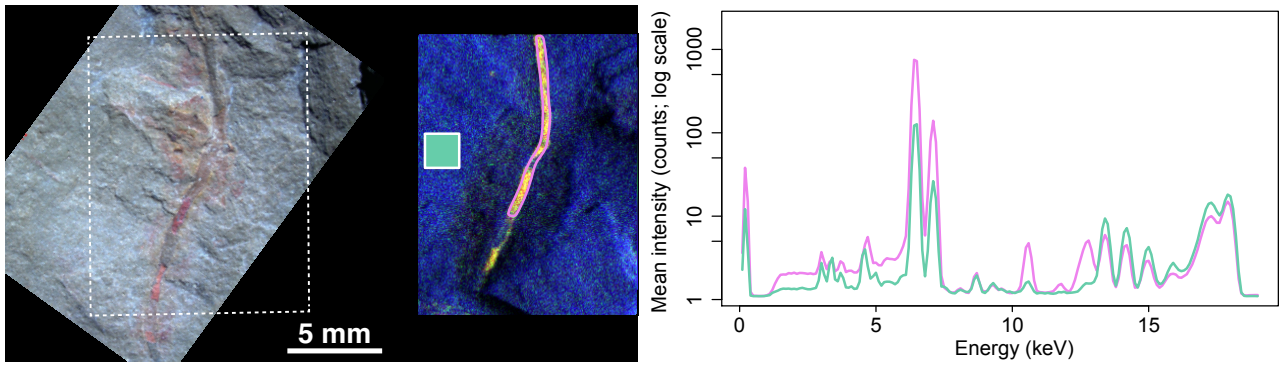
614
 615 **Figure S7. Synchrotron-based XRF major-to-trace elemental mapping of MGL 103593,**
 616 **undescribed "radiodont" appendages from the Early Ordovician Fezouata Shale of Morocco.**
 617 Optical photograph (*left*), false-colour overlays of iron (red), manganese (green), and rubidium
 618 (blue) distributions (*centre*), and the extracted mean XRF spectra from box areas of corresponding
 619 colours in the elemental overlay (*right*). Refer to Fig. 1O for peak identification.

620
 621
 622
 623



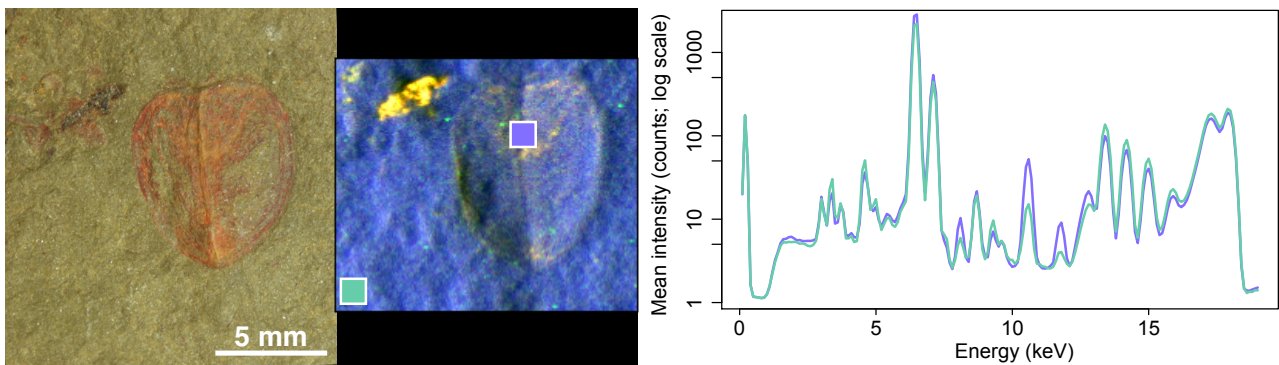
624
 625 **Figure S8. Synchrotron-based XRF major-to-trace elemental mapping of MGL 107866, an**
 626 **undescribed "annelid" from the Early Ordovician Fezouata Shale of Morocco.** Optical
 627 photograph (*top left*), false-colour overlays of iron (red), manganese (green), and rubidium (blue)
 628 distributions (*bottom left*), and the extracted mean XRF spectra from box areas of corresponding
 629 colours in the elemental overlay (*right*). Refer to Fig. 1O for peak identification.

630



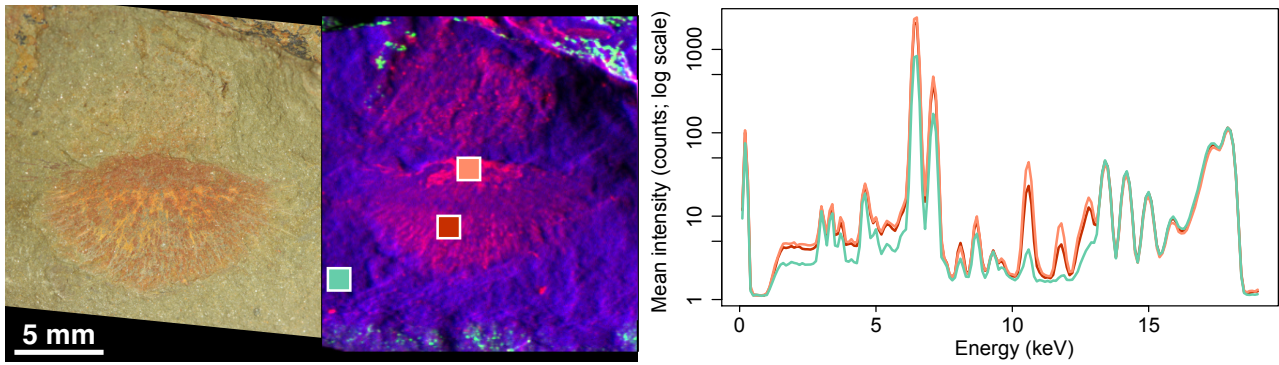
631
632
633
634
635
636
637
638
639
640

Figure S9. Synchrotron-based XRF major-to-trace elemental mapping of AA-TGR1c-OI-47, an undescribed "annelid" from the Early Ordovician Fezouata Shale of Morocco. Optical photograph (*left*), false-colour overlays of iron (red), manganese (green), and rubidium (blue) distributions (*centre*), and the extracted mean XRF spectra from selected areas of corresponding colours in the elemental overlay (*right*). Refer to Fig. 10 for peak identification.



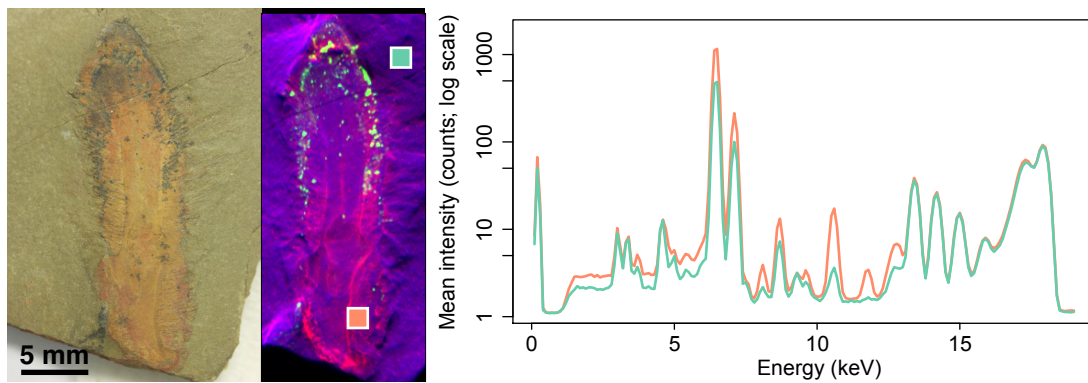
641
642
643
644
645
646
647
648

Figure S10. Synchrotron-based XRF major-to-trace elemental mapping of the marrellomorph euarthropod *Enosiaspis hrungnir* Legg, 2016, specimen MGL 102321, from the Early Ordovician Fezouata Shale of Morocco. Optical photograph (*left*), false-colour overlays of iron (red), manganese (green), and rubidium (blue) distributions (*centre*), and the extracted mean XRF spectra from box areas of corresponding colours in the elemental overlay (*right*). Refer to Fig. 10 for peak identification.



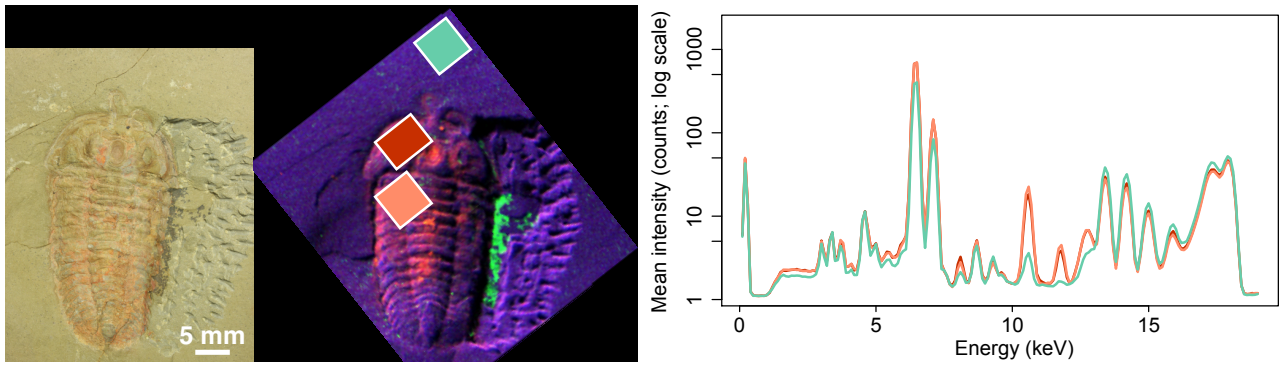
649
650
651
652
653
654
655
656
657
658

Figure S11. Synchrotron-based XRF major-to-trace elemental mapping of the demosponge *Choia sp.*, specimen MGL 107663, from the Early Ordovician Fezouata Shale of Morocco. Optical photograph (*left*), false-colour overlays of iron (red), manganese (green), and rubidium (blue) distributions (*centre*), and the extracted mean XRF spectra from box areas of corresponding colours in the elemental overlay (*right*). Refer to Fig. 1O for peak identification.

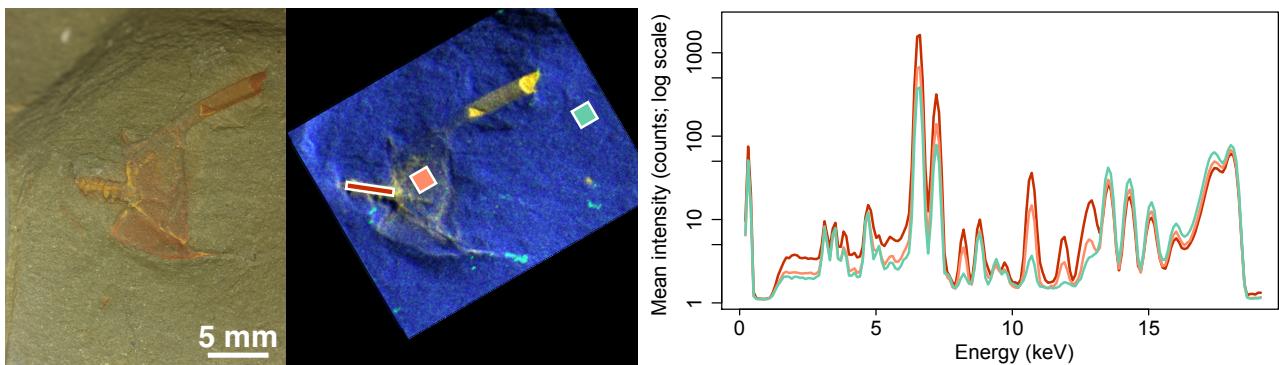


659
660
661
662
663
664
665
666

Figure S12. Synchrotron-based XRF major-to-trace elemental mapping of the demosponge *Pirania auraeum* Botting, 2007, specimen MGL 107764, from the Early Ordovician Fezouata Shale of Morocco. Optical photograph (*left*), false-colour overlays of iron (red), manganese (green), and rubidium (blue) distributions (*centre*), and the extracted mean XRF spectra from box areas of corresponding colours in the elemental overlay (*right*). Refer to Fig. 1O for peak identification.



667
 668 **Figure S13. Synchrotron-based XRF major-to-trace elemental mapping of the trilobite**
 669 ***Bavarilla zemmourensis* Destombes, Sougy & Willefert, 1969, specimen MGL 102222, from the**
 670 **Early Ordovician Fezouata Shale of Morocco.** Optical photograph (*left*), false-colour overlays of iron (red), manganese (green), and rubidium (blue) distributions (*centre*), and the extracted mean
 671 XRF spectra from box areas of corresponding colours in the elemental overlay (*right*). Refer to Fig.
 672 1O for peak identification.
 673
 674
 675
 676
 677

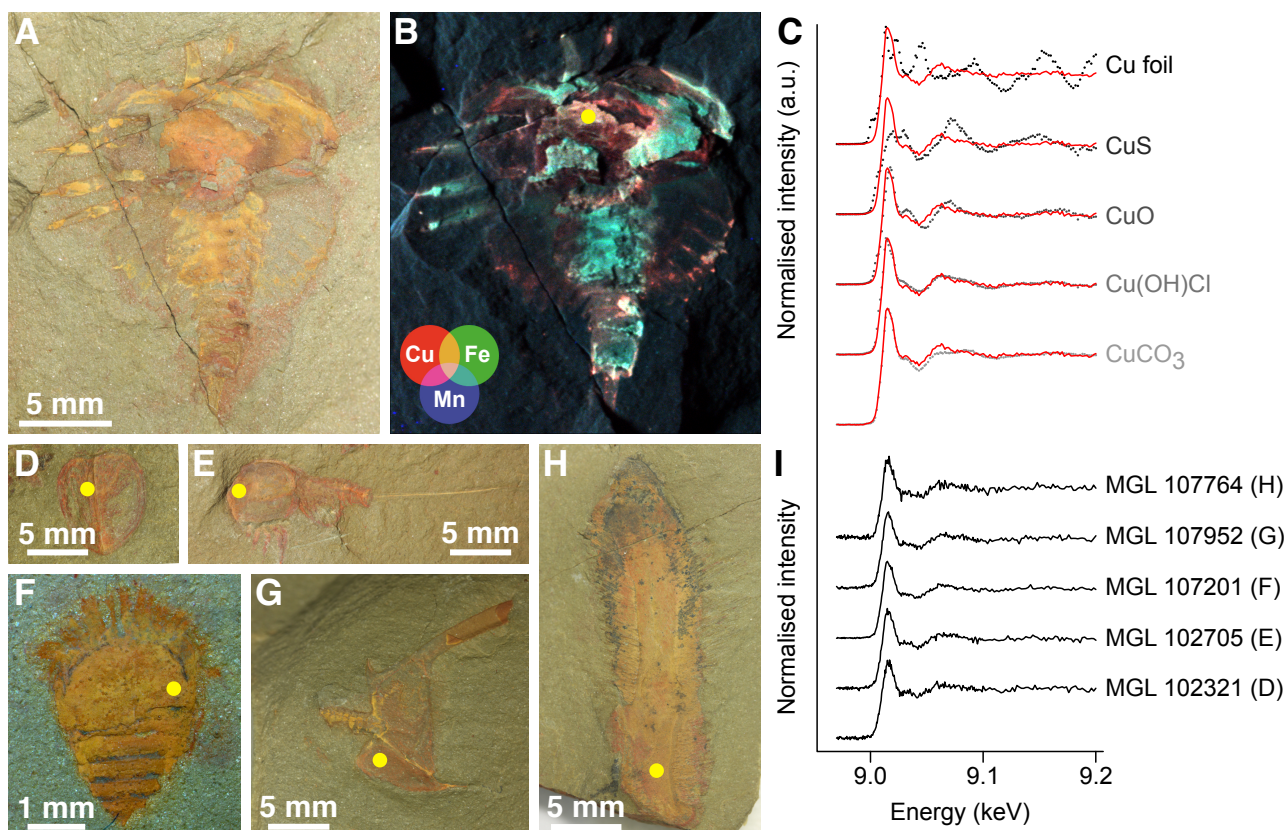


678
 679 **Figure S14. Synchrotron-based XRF major-to-trace elemental mapping of the stylophoran**
 680 **echinoderm *Thoralicystis* sp., specimen MGL 107952, from the Early Ordovician Fezouata**
 681 **Shale of Morocco.** Optical photograph (*left*), false-colour overlays of iron (red), manganese
 682 (green), and rubidium (blue) distributions (*centre*), and the extracted mean XRF spectra from box
 683 areas of corresponding colours in the elemental overlay (*right*). Refer to Fig. 1O for peak
 684 identification.
 685



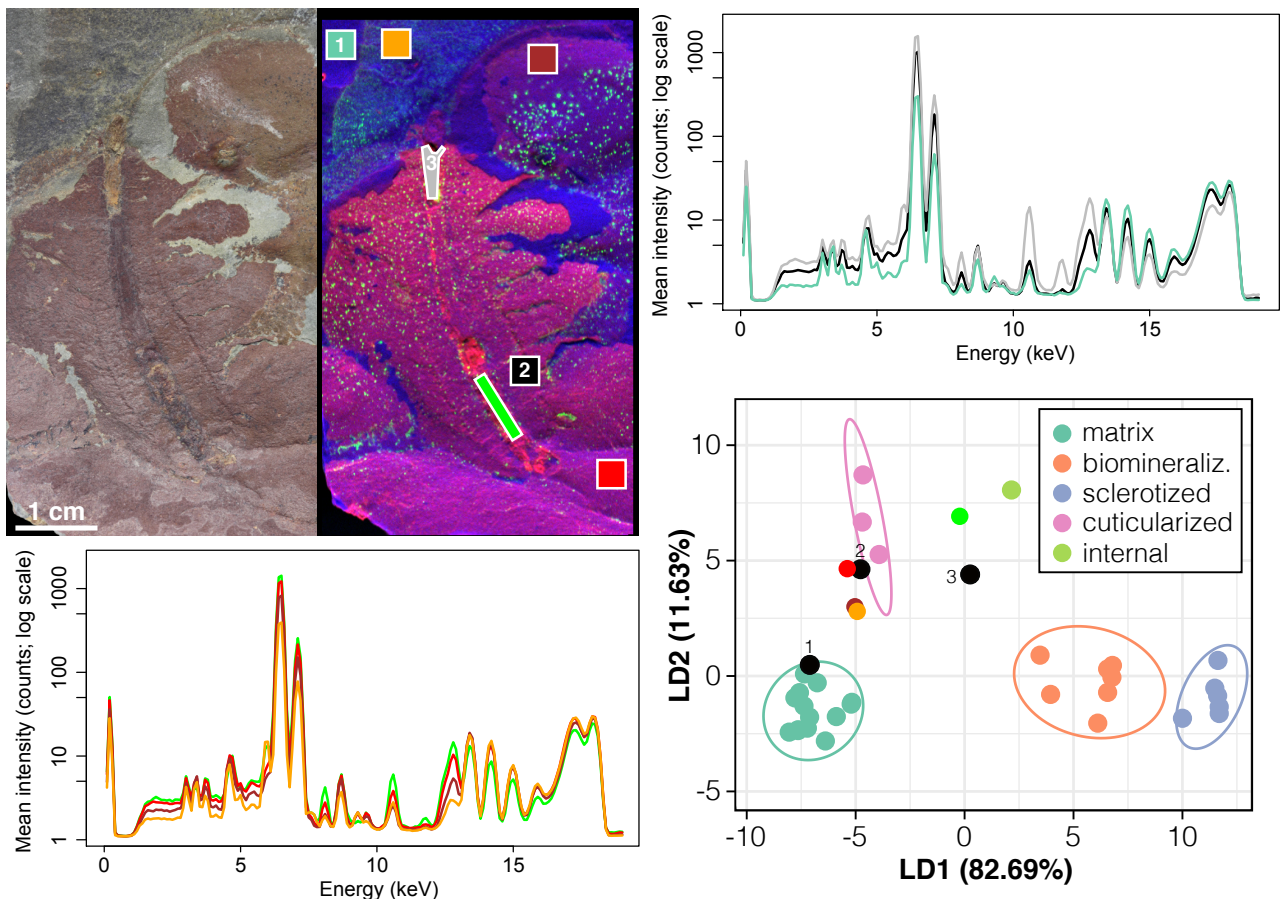
686
 687
 688
 689
 690
 691

Figure S15. Satellite view of the Draa valley locating the different outcrops that yielded the fossils studied herein. The '~14km' measurement refers to the perimeter encompassing all the north localities. Precise locality information is curated with the specimens, and available upon request from the authors.



692
 693 **Figure S16. Synchrotron-based Cu K-edge X-ray absorption spectroscopy (XAS) of a range of**
 694 **fossils from the Early Ordovician Fezouata Shale of Morocco.** (A) Optical photograph of the
 695 undescribed "xiphosuran" MGL 102701. (B) false-colour overlays of copper (red), iron (green), and
 696 manganese (blue) distributions. (C) Cu K-edge XAS spectrum (red line) from the yellow dot in B
 697 superimposed upon spectra collected on reference Cu compounds (grey to black dotted lines) for
 698 comparison. The spectrum obtained for the fossil is inconsistent with metallic copper (Cu), copper
 699 sulfide (CuS) or cupric oxide (CuO) but more consistent with copper hydroxide chloride
 700 (Cu(OH)Cl) and to a greater extent copper carbonate (CuCO₃), suggesting a similar environment for
 701 Cu in the fossil. (D–H) Optical photographs of *Enosiaspis hrungnir* MGL 102321 (D), the
 702 undescribed "xiphosuran" MGL 102705 (E), the undescribed "synziphosurine" MGL 107210 (F),
 703 *Thoralicystis sp.* MGL 107952 (G), and *Pirania auraeum* MGL 107764 (H). (I) Cu K-edge XAS
 704 spectra from the yellow dot in D–H, showing that Cu is present in all investigated fossils in the
 705 same chemical environment. XAS was performed at the DiffAbs beamline (SOLEIL synchrotron)
 706 with the following acquisition parameters: fluorescence mode, 230×150 μm² (H×V) beam spot size,
 707 3 s counting time per energy step; energy step sizes were 0.5 eV between 8970 and 9030 eV, 1 eV
 708 between 9031 and 9100 eV, and 2 eV between 9102 and 9200 eV. Spectra have been normalised,
 709 and the references corrected from self-absorption, using the Athena software⁶⁸.

710
 711 68. B. Ravel, M. Newville, ATHENA, ARTEMIS, HEPHAESTUS: data analysis for X-ray
 712 absorption spectroscopy using IFEFFIT. *Journal of Synchrotron Radiation* **12**, 537–541
 713 (2005).
 714



715
 716 **Figure S17. Synchrotron-based X-ray fluorescence major-to-trace elemental mapping of AA-**
 717 **FETB-OI-22, an undescribed “enigmatic organism” from the Early Ordovician Fezouata**
 718 **Shale of Morocco.** (Top left) Optical photograph. (Top centre) False-colour overlays of iron (red),
 719 manganese (green), and rubidium (blue) distributions. (Top right) Mean XRF spectra from the box
 720 areas of corresponding colours (numbered 1 to 3) in the elemental overlay, corresponding to the
 721 same areas as in Fig. 2C. (Bottom left) Additional mean XRF spectra, extracted from the orange,
 722 brown, red (weathered matrix) and green (other internal remains) box areas of corresponding
 723 colours in the XRF false-colour overlay. Refer to Fig. 10 for peak identification. (Bottom right)
 724 Classification of the all 7 extracted XRF spectra within our linear discriminant analysis. Note that
 725 weathered matrix spectra plot closer to cuticularized tissues the richer they are in iron, following the
 726 fact that the shale matrix (clay and silica) is way less concentrated in iron than the fossil tissues
 727 (iron oxides). Of note is also the classification of the green XRF spectrum, corresponding to the
 728 remains of an internal system, which plots close to the trilobite internal, most likely digestive,
 729 tissue, suggesting that this area may preserve remains of the digestive system.
 730
 731

Taxon	Collection number	Locality	Figure(s)	Spectrum	Tissue type (Following [35])	XRF map scan step (μm)	XRF map dwell time (ms)	Number of pixels selected	Time over slected area (s)
undescribed "xiphosuran"	MGL 102701	A5 (2015)	Figs. 1A, S1	1	sclerotised	20	25	900	22.5
				2	matrix	20	25	900	22.5
undescribed "synziphosurine"	MGL 107210	A16 (2015)	Figs. 1B, S2	1	sclerotised	20	20	1122	22.44
				2	matrix	20	20	1122	22.44
undescribed "synziphosurine"	MGL 102841	"Synz. Loc."	Figs. 1C, S3	1	sclerotised	20	20	1122	22.44
				2	matrix	20	20	1122	22.44
undescribed "marrellid"	AA-BIZ31-OI-39	ZF4(31)	Figs. 1D, S4	1	sclerotised	70	70	324	22.68
				2	matrix	70	70	324	22.68
undescribed "xiphosuran"	MGL 102705	A5 (2015)	Figs. 1E, S5	1	sclerotised	70	50	441	22.05
				2	matrix	70	50	441	22.05
<i>Bavarilla zemmourensis</i> Destombes. Sougy & Willefert. 1969	MGL 102177	A17 (2015)	Figs. 1F, S6	1	internal	70	20	1128	22.56
				2	matrix	70	20	1122	22.44
undescribed "radiodont" appendages	MGL 103593	A27 (2016)	Figs. 1G, S7	1	cuticularised	70	25	900	22.5
				2	matrix	70	25	900	22.5
undescribed "annelid"	MGL 107866	A2 (2015)	Figs. 1H, S8	1	cuticularised	70	20	1127	22.54
				2	matrix	70	20	1122	22.44
undescribed "annelid"	AA-TGR1c-OI-47	ZF51c	Fig. S9	1	cuticularised	70	20	1124	22.48
				2	matrix	70	20	1122	22.44
<i>Enosiaspis hrungnir</i> Legg. 2016	MGL 102321	A6 (2015)	Figs. 1I, S10	1	sclerotised	70	60	380	22.8
				2	matrix	70	60	380	22.8
<i>Choia</i> sp. (Botting 2007)	MGL 107663	A17 (2015)	Figs. 1J, S11	1	biomineralised	70	50	441	22.05
				2	biomineralised	70	50	441	22.05
				3	matrix	70	50	441	22.05
<i>Pirania auraeum</i> Botting. 2007	MGL 107764	A26 (2016)	Figs. 1K, S12	1	biomineralised	70	40	552	22.08
				2	matrix	70	40	552	22.08

<i>Bavarilla zemmourensis</i> Destombes. Sougy & Willefert. 1969	MGL 102222	A16 (2015)	Figs. 1L, S13	1	biomineralised	200	20	1122	22.44
				2	biomineralised	200	20	858	17.16 **
				3	matrix	200	20	1122	22.44
<i>Thoralicystis</i> sp. (Lefebvre et al. 2019)	MGL 107952	A9 (2015)	Figs. 1M, S14	1	biomineralised	70	30	729	21.87
				2	biomineralised	70	30	638	19.14 **
				3	matrix	70	30	729	21.87
undescribed "enigmatic organism"	AA-FETB-OI-22	ZF2(3b)	Figs. 2, S17	1	?	100	20	1122	22.44
				2	?	100	20	1124	22.48
				3	matrix	100	20	1122	22.44
				4	weathered matrix	100	20	1122	22.44
				5	weathered matrix	100	20	1122	22.44
				6	weathered matrix	100	20	1122	22.44
				7	?	100	20	1121	22.42

Table S1. Details on the specimens, acquisition parameters and selected spectra studied herein. (** Denotes 2 spectra for which it was not possible to obtain a collection time over the selected area close to 22.5 s)

Element	Sclerotised	Biom mineralised	Cuticularised
K	0.5112	1.956	0.4588
Ca	0.5725	0.5226	0.3237
Ti	0.1771	0.8605	0.2255
Cr	0.03413	0.04596	0.03328
Mn	0.2118	0.2076	0.2984
Ni	0.03054	0.03625	0.08007
Cu	0.3035	0.2087	0.02415
Zn	0.2127	0.4004	0.2436
Ga	0.007206	0.05585	0.01741
As	0.6792	0.522	0.04578
Br	0.006563	0.00397	0.0003272
Rb	0.2398	0.4184	0.1613
Sr	0.1391	0.2448	0.09511
Y	0.007973	0.03406	0.01968
Pb	0.5217	0.3441	0.3683

732

733

734

735

Table S2. XRF minor to trace element quantification of the mean spectra for the sclerotized, biom mineralized and cuticularized tissues (wt%)